Review article

Nuclear Medicine Communications

A review of PET normalization: striving for count rate uniformity

Lampros Theodorakis[a,c], George Loudos[c], Vasilios Prassopoulos[d], Constantin Kappas[b], Ioannis Tsougos[b] and Panagiotis Georgoulias[a]

The advent of PET instrumentation signaled the beginning of a new perspective in nuclear medicine diagnostic imaging. PET systems rely on several corrections that must be applied in order to establish accurate and reliable quantification. The inherent properties of PET detector architecture and the crystals themselves are sources of different types of systematic and random errors with subsequent count rate variability that should be accounted for. Normalization is the correction dealing with these errors. In this work, the reasons resulting in this variability are explored and the different normalization approaches are described. Special focus is paid to component-based normalization, with an attempt to describe the discrete factors and discuss the underlying mechanisms of their contribution to sensitivity variations of the lines of response. *Nucl Med Commun* **34:1033–1045 © 2013 Wolters Kluwer Health | Lippincott Williams & Wilkins.**

Nuclear Medicine Communications 2013, **34:**1033–1045

Keywords: normalization, PET/CT, quantification

[a]Department of Nuclear Medicine, University Hospital of Larissa, [b]Department of Medical Physics, Medical School, University of Thessaly, Larissa, [c]Department of Medical Instruments Technology, Technological Educational institute of Athens and [d]Department of PET/CT, Hygeia Hospital, Athens, Greece

Correspondence to Panagiotis Georgoulias, MD, PhD, Department of Nuclear Medicine, University Hospital of Larissa, Larissa 41110, Greece
Tel: +30 241 350 2918; fax: +30 241 350 1863;
e-mail: pgeorgoul@med.uth.gr; georgoulias@hotmail.com

Received 27 March 2013 **Revised** 21 July 2013 **Accepted** 7 August 2013

Introduction

The advent of PET instrumentation signaled the beginning of a new perspective in nuclear medicine diagnostic imaging [1–3]. The PET scanner is the descendent of single photon emission computed tomography systems in tomography, introducing whole-body images with spatial resolution in the order of millimeters [4]. The initial diagnosis and restaging of cancer is supported by precise quantification of the distribution of radiopharmaceuticals in the human body, revealing functional information on specific organs and tissues to the physician [5,6]. Moreover, dual-modality PET/computed tomography (CT) systems resulted in a fused image, combining the advantages of the functional information obtained from the PET scanner and the anatomical information obtained from the CT system [7]. Exact registration of the two images offers better localization of a malignant lesion, whereas quantification tools show the extent of malignancy or the degree of response to treatment in the case of restaging examinations after chemotherapy or radiotherapy treatment (Fig. 1).

PET systems rely on several corrections that must be applied for this quantification to be accurate and reliable [8–11]. The most prominent of these corrections is attenuation correction. The ability to accurately correct for attenuation in PET was one of the first developments that considerably improved the final images, when compared with those obtained with single photon emission computed tomography. This fact was further pointed out with the introduction of PET/CT systems adopting CT-based attenuation correction [12]. However, the calculation of attenuation values from CT transmission images will result in overcorrection or undercorrection in some cases, and this is often reported in the literature [13].

Except for attenuation, common correction schemes with other modalities (scatter correction, dead-time estimation), and other 'PET specific' corrections (randoms correction), are also crucial for qualitative and quantitative results [14,15].

The inherent properties of PET detector architecture and the crystals themselves are sources of different types of systematic and random errors that should be accounted for. Normalization is the correction dealing with these errors [16–18]. Figure 2 illustrates the necessity to perform the normalization correction accurately in clinical scanners. A poorly normalized PET detector will severely deteriorate the diagnostic value of the images produced.

Each scanner model follows a specific protocol in order for the technologist or the service engineer to normalize the detector. In older systems the steps of the protocol are carried out periodically on the basis of the manufacturer's specifications (i.e. on a monthly basis), whereas newer systems include normalization as part of their daily quality-check process.

A number of factors affect lines of response (LOR) efficiency in various ways, producing subsequent LOR count rate variability. Normalization is applied during reconstruction and corrects for this variability.

In this work, the reasons resulting in this variability have been explored and the different normalization approaches have been described. Special focus has been paid to

0143-3636 © 2013 Wolters Kluwer Health | Lippincott Williams & Wilkins DOI: 10.1097/MNM.0b013e328365ac1e

Fig. 1

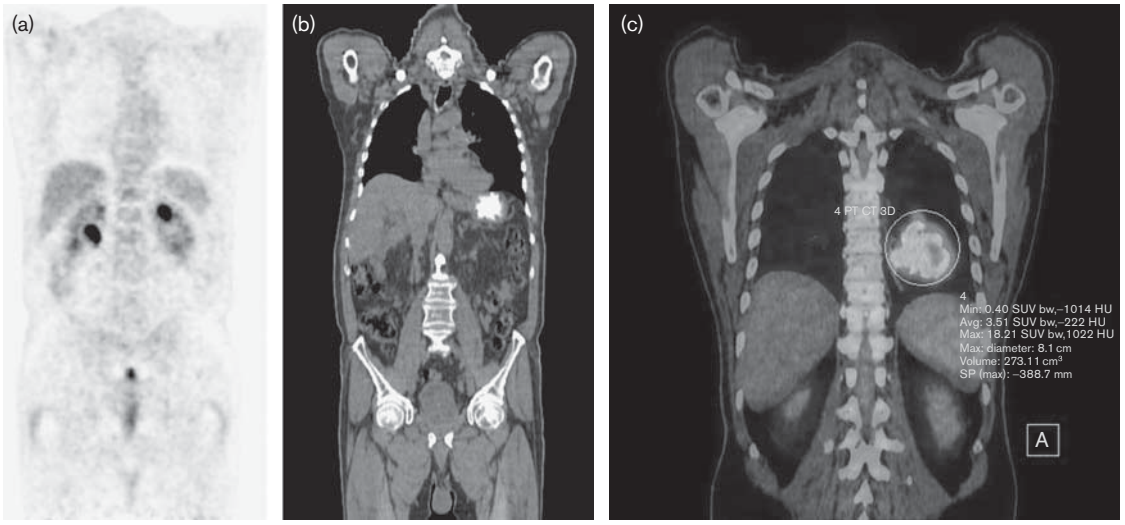

(a) Metabolic image from PET is registered to (b) anatomic computed tomography (CT) image. (c) Malignant lesion visualization with fused PET/CT images.

Fig. 2

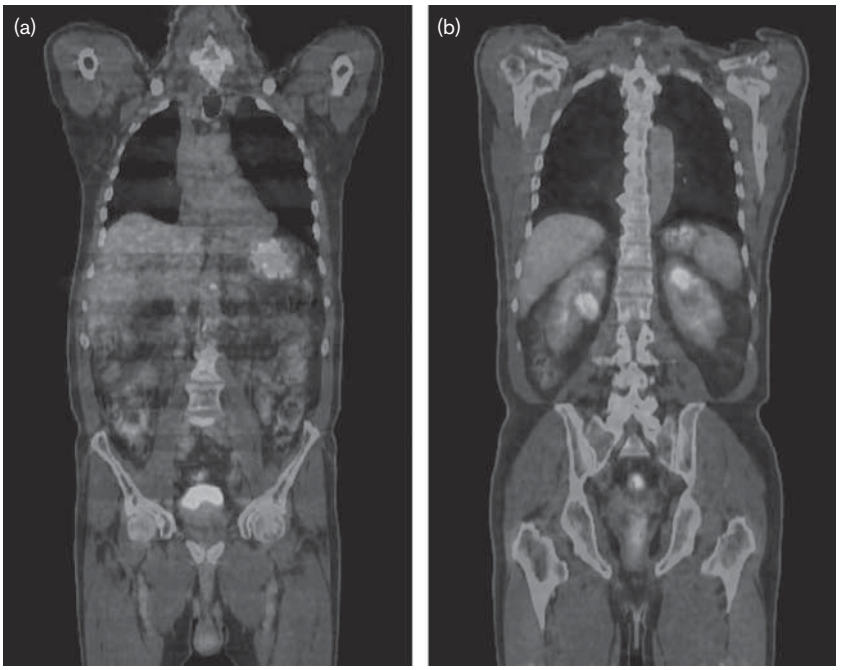

Comparison of (a) a non-normalized coronal whole-body image with (b) a normalized one. Axial band artifacts are shown in the former case.

component-based normalization, with an attempt to describe the discrete factors and discuss the underlying mechanisms of their contribution to sensitivity variations of the LOR. Component-based normalization has been the method of choice for the majority of clinical and research PET scanners. The algorithm went through successive versions of higher complexity following the introduction of more complex detectors. The explanation of the above factors is followed by a brief and mostly historical presentation of how the researchers dealt with normalization. The authors believe that such an overview will offer the reader the chance to relate the factors in the

algorithm with the technological advances that point out the need to incorporate these factors in the model.

Direct normalization

Normalization is applied to counteract on count rate variability in LOR sensitivity. It aims to build normalization sinograms to be applied to the activity sinograms. A single entry in the sinogram represents a combination of LORs due to raw data compression schemes. The purpose of the normalization sinogram is to correspond a normalization factor (NF_{ijuv}) to each one of the resultant LORs connecting crystals i and j from crystal rings u and v, respectively. Then, the total NF for the case of a combination of LORs would be the product of the factors for each LOR. The variability is due to a number of factors that are described hereinafter. In a theoretical case, if it would be somehow known *a priori* that a source of known shape and position in the PET field of view (FoV) is equally illuminating all crystal pairs forming an LOR (A is the activity of the source), that proper attenuation, scatter, and random corrections have been applied, and that there are no sensitivity variance effects, then with C_{ijuv} (cps) being the count rate measured in the LOR for detector pair i (crystal ring u) and j (crystal ring v):

$$C_{ijuv} = A\,(\text{constant})(i,j \in 1...N),\ |u-v| \leq \text{MRD}, \quad (1)$$

where MRD is the maximum ring difference between crystals that the system accepts coincidences from.

However, this is not the case in reality. A number of factors (F_{ijuv}) affect LOR sensitivity and the count rate is different for detector pairs:

$$C_{ijuv} = F_{ijuv} \times A. \quad (2)$$

The NF_{ij} counteract on the effect of F_{ijuv}:

$$NF_{ijuv} = 1/F_{ijuv}. \quad (3)$$

It is shown from the equations above that the count rate C_{ijuv} can be measured directly during a calibration scan and the calculation of NF_{ijuv} is straightforward:

$$NF_{ijuv} = \text{A}/C_{ijuv}. \quad (4)$$

This method is known as direct normalization.

Activity correction

In Eqs (1)–(4) the theoretical source is still assumed. In reality, the cylindrical geometry of the PET detector results in different levels of activity 'seen' by each LOR. A way to overcome this is by using different shapes of volume sources and correcting for this difference. This is called activity correction. For example, in Fig. 3, detectors 1 and 3 and detectors 2 and 4 belong to the same ring and form LOR_{13} and LOR_{24}, respectively. A plane source of uniform activity is placed at the center of the FoV. The total length of activity 'seen' by LOR_{13} and LOR_{24} is $A_{13} = a$ and $A_{24} = b$, respectively, and if C_{13} and C_{24} are the two count rates then $\frac{C_{13}}{C_{24}} = \cos\theta$. The active lengths (part of the LOR traversing 'hot' source material) for the two LORs are then $\text{LOR}_{13\text{act}} = a$ and $\text{LOR}_{24\text{act}} = a/\cos\theta$. In that case, for crystals i and j:

Fig. 3

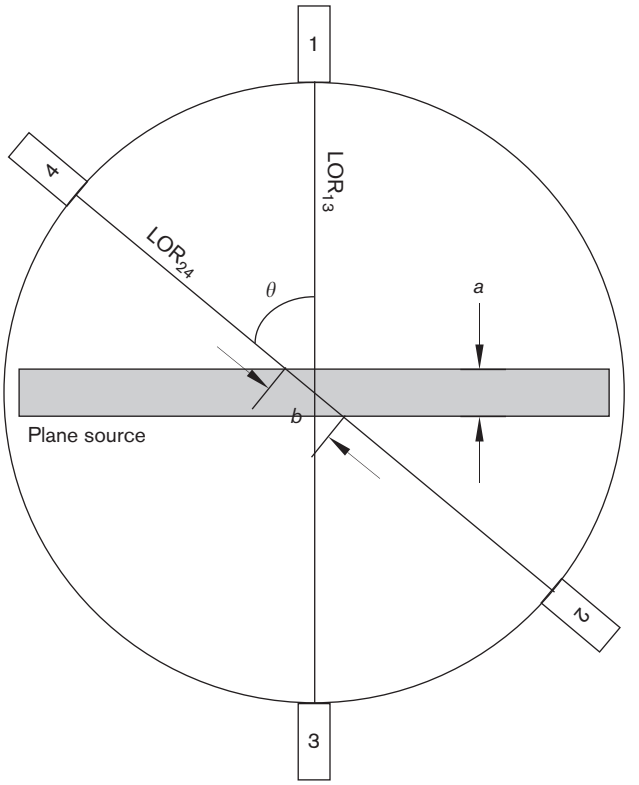

Transaxial activity correction for the case of a plane source for a single ring detector.

$A_{ij} = A/\cos\theta$, where A_{ij} is the activity correction (A_{corr}) term replacing the term A in Eqs (1)–(4).

Similar activity corrections can be applied for sources of other geometry, both transaxially and axially if there is more than one ring detector [19].

Component-based normalization

The transition from two dimensional (2D) to three dimensional (3D) scanning resulted in a 10-fold increase in the number of LORs [20]. This fact made the use of direct normalization impractical. Equation (4) states that in order to apply the model the individual count rate C_{ijuv} should be measured independently. This would result in an enormous computational load and a massive amount of time to normalize the detector accurately. The use of high-activity sources to reduce time by increasing the count rate is also not applicable because of the respective increase in dead-time and pulse pile-up effects [21]. Moreover, the factor F_{ijuv} affecting LOR sensitivity is the numerical representation of the total count rate variability effect, which in turn can be subdivided into several components. Each component

contributes differently according to its nature. For example, the detector geometry component G_{uvr} (r being the distance of LOR_{ij} from the center of FoV) or, in other words, the effect of how the block detectors are arranged mechanically in a cylindrical detector system is a steady component that should be calculated only once and remains the same thereafter. Conversely, the efficiency drift of the scintillating crystal ϵ_{ijuv} is an inherent property that changes with the detector aging and should be calculated periodically in time. For the case of a component-based normalization model consisting of only these two effects:

$$F_{ijuv} = G_{uvr} \times \varepsilon_{ijuv}. \quad (5)$$

The efficiency of any crystal pair is equal to the product of the respective efficiencies of each crystal:

$$\varepsilon_{ijuv} = \varepsilon_{iu} \times \varepsilon_{jv}. \quad (6)$$

Then, from Eqs (3), (5), and (6):

$$N_{ijuv} = (G_{uvr} \times \varepsilon_{iu} \times \varepsilon_{jv})^{-1}. \quad (7)$$

This concept gave birth to a new normalization approach, named after component-based normalization [22]. The algorithm was first introduced in its simplified form [Eq. (7)], but has been developed since then and incorporates several other factors. Equation (8) includes all the factors and is followed by an overview of their names. In the following paragraphs, each factor is explained separately. A brief explanation of the underlying mechanisms with which each factor contributes to LOR sensitivity variation is also attempted. The explanation is given with the aid of a detector setup, which is used as an example for the calculation of the factors (Fig. 4a):

$$C_{ijuv} = \varepsilon_{iu} \times \varepsilon_{jv} \times G_{uvr} \times P_{uv} \times b_{LOR_{ijuv}} \times \mu_{LOR_{ijuv}} \times d_{uvrk} \times t_{iuvj} \times A_{corr}, \quad (8)$$

C_{ijuv} is the count rate of the crystal pair formed by crystal i in ring u and crystal j in ring v; ε_{iu} and ε_{jv} are the inherent crystal efficiencies of crystals i and j, respectively; G_{uvr} is the radial geometric factor for LOR distance from the center of the FoV equal to r; P_{uv} is the plane efficiency factor defined by any LOR connecting crystals from rings u and v; $b_{LOR_{ijuv}}$ is the total transaxial block efficiency of the LOR connecting crystal i from ring u with crystal j from ring v; $\mu_{LOR_{ijuv}}$ is the total axial block efficiency of the LOR connecting crystal i from ring u with crystal j from ring v; d_{uvrk} is the crystal interference factor for a crystal with index k ($k = 1 \ldots D$) for the case of a block detector with D transaxial crystals in the block; t_{ijuv} is the time alignment factor; A_{corr} is the activity 'seen' by the LOR connecting crystal i from ring u and crystal j from ring v.

The measurements performed for the determination of the NFs utilize volume sources of different shapes (cylindrical, plane, or line sources), filled with homogeneous long-lived radioactive materials (^{68}Ge). For the calculations described below, it is assumed that the shape, size, and activity of the source corrected for time decay are accurately known. The raw data for the normalization scans are also assumed to be corrected for attenuation, randoms, and scatter.

Factors of component-based normalization

Inherent crystal efficiency (ε_{iu}, ε_{jv})

The efficiency of a scintillator crystal demonstrates its ability to convert γ photons into light. This ability depends on several factors, the most important of them

Fig. 4

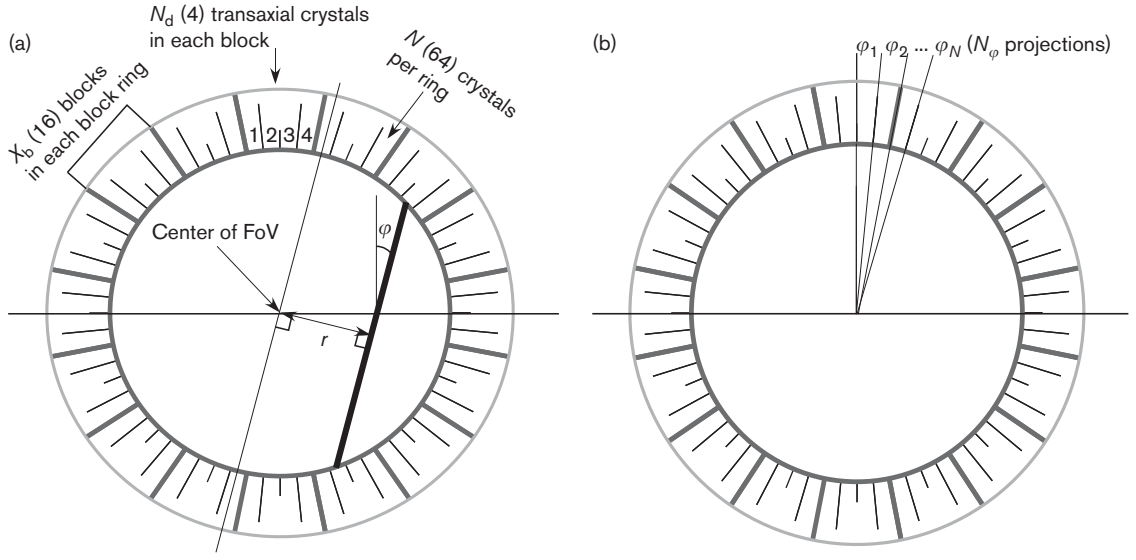

The example detector with (a) the notation of the parameters and (b) the corresponding projections. FoV, field of view.

being the compound uniformity of the scintillator material and the crystal volume. Impurities deteriorate the efficiency, whereas higher crystal volumes result in efficiency increase. The crystals being part of the block structures are mostly equal in size; however, there are some cases reported in the literature where the edge and corner detectors are cut slightly smaller than the other detectors in order to satisfy design demands [23]. Moreover, in the case of two crystals of the same volume, the amount of scintillation light produced is strongly dependent on the area/length ratio of the elements, and even small differences among them could also result in efficiency variations. The temperature-dependent and hygroscopic nature of certain scintillators can lead to additional variations, taking into account the fact that environmental conditions inside the gantry could be slightly different over time or in different areas [24].

Except from the crystal properties, random efficiency variation could also arise because of photomultiplier tube (PMT) or avalanche photodiode (APD) gain variations. Small discrepancies between the high voltages applied to the ends of the PMT, for example, are followed by different amplification factors for the electrons between successive dynodes. The resulting pulses will carry these discrepancies, and certain groups of crystals will show to be more efficient than others.

Fig. 5

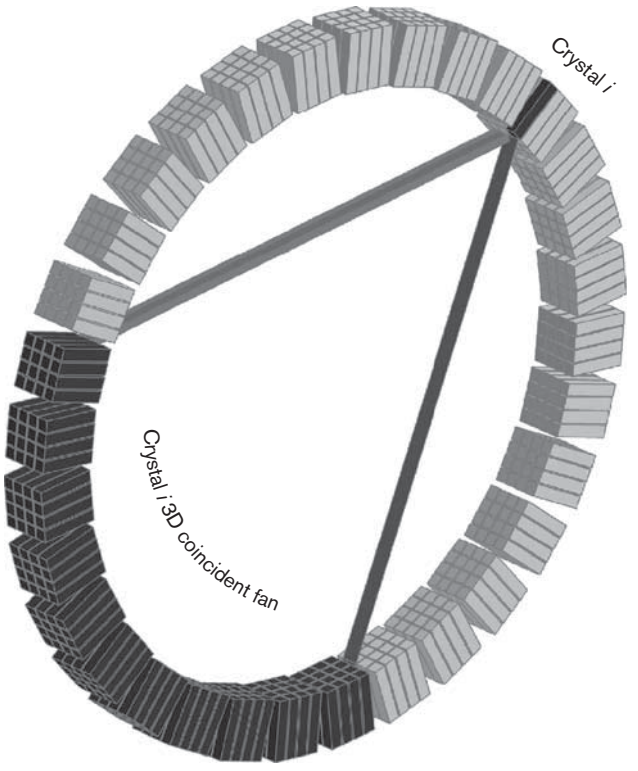

The three dimensional (3D) fan sum algorithm assumes that the sum of efficiencies in the coincident fan of crystal *i* (shown in black) is constant for all the created fans in the detector.

The inherent crystal efficiency calculation is based on the 3D fan sum algorithm [25]. The idea behind the calculation is that the total count rate of the 3D fan that each crystal coincides with is approximately equal to a constant. The fan sum algorithm was first introduced in its single-plane version but has since been developed for application in 3D acquisition modes. If A is the 3D coincident fan in Fig. 5 formed by crystal i and crystal j in the fan, then for the crystal efficiency ϵ_{iu}:

$$\varepsilon_{iu} = \frac{\varepsilon_{iu} \sum_{v \in A} \sum_{j \in A} (\varepsilon_{jv})}{\sum_{v \in A} \sum_{j \in A} (\varepsilon_{jv})}. \quad (9)$$

If the approximations are valid, the denominator of the equation will be approximately equal to a known constant. This is actually valid because the differences in crystal efficiencies in the fan will vary around unity in such a way that they will ultimately cancel out. The numerator is obtained from the experimental data (normalization scan), and the same calculation is performed for all the rings. This way, a similar equation is determined for the inherent efficiency of crystal j from ring v:

$$\varepsilon_{jv} = \frac{\varepsilon_{jv} \sum_{u \in A} \sum_{i \in A} (\varepsilon_{iu})}{\sum_{u \in A} \sum_{i \in A} (\varepsilon_{iu})}. \quad (10)$$

Transaxial and axial block profile ($b_{LOR_{ijuv}}$ and $\mu_{LOR_{ijuv}}$)

The efficiency of an LOR connecting crystal i in ring u with crystal j in ring v varies with respect to a combination of two effects. The first is with respect to the transaxial index k of the crystals i and j relevant to the block where they belong. For the case of a block consisting of $D \times D$ crystal (D transaxial and D axial crystals), if $D = 4$ then $k = 1 \ldots 4$ (Fig. 6a). The second is with respect to the specific rings u and v where the two crystals belong. Referring to Fig. 6b, crystal i ($k = 1$ and $u = 4$) will have a different block efficiency, b_{iuk}, compared with the one of crystal j, b_{jvk} ($k = 2$, $v = 2$). The block profile factor is a manifestation of pulse pile-up effects. Crystal efficiencies in the block will vary for the case of different count rates experienced by the block due to dead-time response. The block profile correction factor was first introduced by Badawi *et al.* [26], although Casey *et al.* [27] first recognized the need for a dead-time correction during normalization. The difference in the approaches was that Casey and colleagues suggested an empirical 'dead-time' correction that combined paralyzing and nonparalyzing effects. Badawi and colleagues, in contrast, proposed calculating the sum of the efficiencies for crystals with the same k index for each ring and divide

Fig. 6

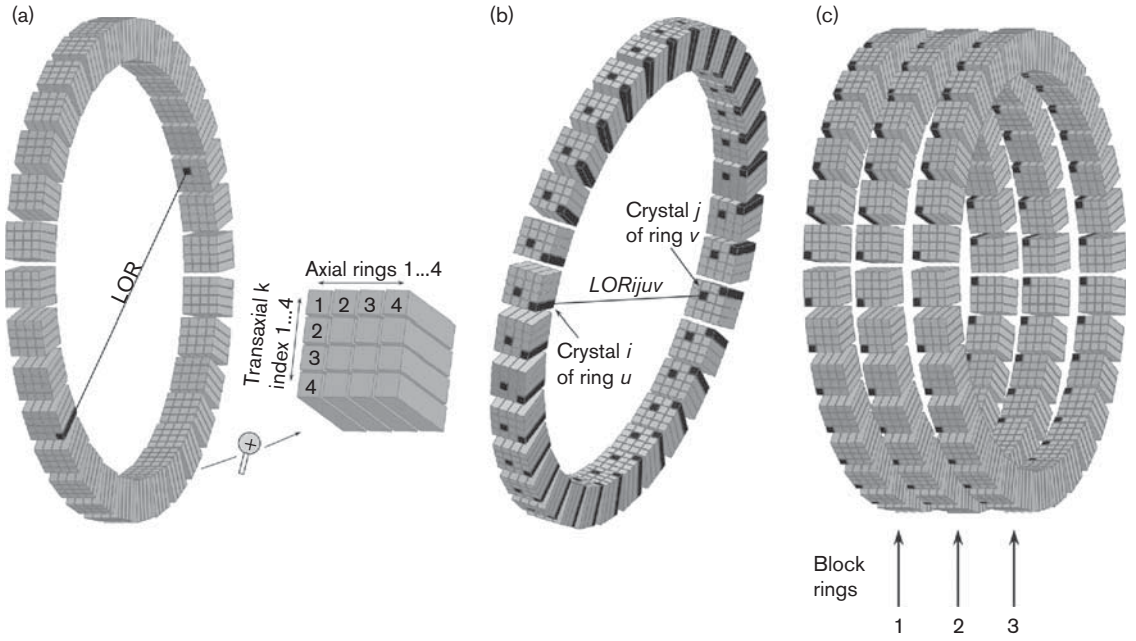

(a) LOR_{ijuv} connects crystal i with k index equal to1 and axial ring index u equal to 4. (b) The same indexes for crystal j are $k=2$ and $v=2$. The block profile calculation includes the summation of the efficiencies of crystals with the same transaxial index in the ring to which they belong (blackened crystals). (c) Detector consisting of three axial block rings. LOR, lines of response.

the result with their number:

$$b_iuk = \frac{\sum_{n=1}^{N/D} \varepsilon_{u,nD+k}}{N/D} (k \text{ being the index of crystal } i). \quad (11)$$

$$b_{\bar{v}j}k = \frac{\sum_{n=1}^{N/D} \varepsilon_{v,nD+k}}{N/D} (k \text{ being the index of crystal } j). \quad (12)$$

The total block LOR efficiency $b_{LOR_{ij}}$ connecting the two crystals is the product of the above equations:

$$b_{LOR_{ijuv}} = b_{uik} \times b_{vjk} = \frac{\sum_{n=1}^{N/D} \varepsilon_{u,nD+k} \times \sum_{n=1}^{N/D} \varepsilon_{v,nD+k}}{(N/D)^2}. \quad (13)$$

Initial estimates for the crystal efficiencies ε_{iu} and ε_{jv} for the calculation are provided by the 3D fan sum algorithm described above. The same methodology is followed for the calculation of the axial block profile ($\mu_{LOR_{ijuv}}$) where:

$$\mu_{LOR_{ijuv}} = \mu_{uiz} \times \mu_{vjz}. \quad (14)$$

The difference is that, for the axial calculation, Z is considered axially, following the axial rings index (Fig. 6a, $Z = 1 \ldots 4$). The axial block profile is essential for the case of more than one block ring in the detector (Fig. 6c).

A number of factors contribute to block profile variations both axially and transaxially. Scatter in the block is one of them. The fraction of correctly identified events in the block level decreases, while moving toward the middle crystals of the block. The crystal identification algorithms fail to register the events correctly, and because of pulse pile-up they eventually misregister with a tendency toward the middle. For the case of PMT, cross-talk through the glass of the PMT has also been reported [23]. Finally, the coverage of the crystals from the PMT or the APD is also an important source of systematic error in efficiency, with some crystals in the block being more covered compared with others in the same block (Fig. 7a and b). All of these reasons outline the need for block profile correction.

Self-normalization: The block profile already mentioned as part of the component-based normalization is a manifestation of pulse pile-up. The number of piled up events, however, is severely affected by the count rate with which the block assembly is loaded. The higher the activity, the higher the count rate and higher the number of pile-up events experienced. Therefore, count rate discrepancies between the normalization scans – irrespective of the setup used – and the emission scan itself can lead to high-frequency artifacts. Badawi *et al.* [28] investigated a method for tackling these artifacts. The corresponding block profile normalization components consist of a transaxial component ($b_{LOR_{ijuv}}$) and an axial one ($\mu_{LOR_{ijuv}}$), as already shown in Eq. (8). On the basis of this method, taking some basic assumptions into account, the transaxial component could be calculated from ordinary emission data rather than from data from a separate normalization scan. The basic idea is that the transaxial block profile factors are calculated with Eq. (13), although not with a normalization scan using

Fig. 7

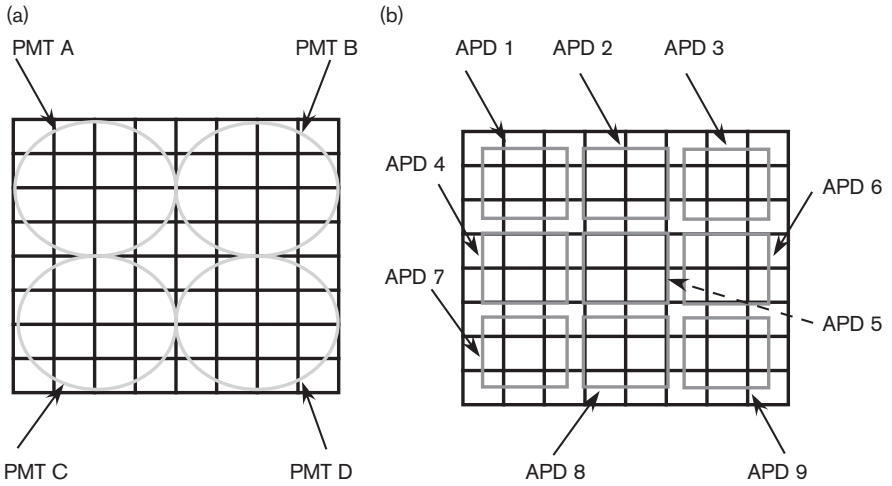

Some crystals in the block (8 × 8 total crystals shown here) are fully covered by (a) the photomultiplier tube (PMT) (four circular PMTs shown here) (b) or the avalanche photodiode (APD) (nine rectangular) (b), whereas some others are not. The effect varies with respect to the block design.

a volume source but with the emission data set (i.e. a head scan). Badawi and colleagues proved experimentally that such a preprocessing normalization step reduces the mentioned artifacts.

The concept of self-normalization is also mentioned in a later study by Ishikawa *et al.* [29]. The authors adjusted the model for the case of a continuous 3D scanning system. In their case, the transaxial block profile factors and the crystal efficiencies were also calculated from the emission data but with continuous bed movement during scanning. In contrast to step-and-shoot scanning, continuous bed movement simplifies normalization, in the sense that the LOR variance due to axial geometric factors is minimal. In this case, the elements in the axial direction are summed in plane, and count differences between them are ruled out. This is not the case, however, in step-and-shoot modes exploited by the vast majority of clinical PET scanners today. Generally, self-normalization aims to obviate the need for excessive normalization scans. However, further proof from experimentation of the algorithms with clinical data is considered necessary, especially *in vivo*.

Plane efficiency P_{uv}

There are Z^2 axial planes for a multiring detector consisting of Z axial rings (Fig. 6a). Each plane is defined by LOR connecting crystals either from the same or from different crystal rings and has a different overall efficiency. The plane efficiency factor is applied to every LOR in the plane – that is, for every distance from the center and for every view angle. This factor encompasses sensitivity variations between planes that arise because of incidence angle effects and solid angle subtended as a function of ring difference. Count density of direct planes, for instance, is different from the one of oblique planes. For the calculation of the factors the counts in all LORs and all planes (all ring combinations) are summed and the result is divided by Z^2. This is the average plane count rate $\frac{1}{Z^2}\sum_{u,v}\sum_{r,\varphi} S(r,\varphi,u,v)$, where $S(r,\varphi,u,v)$ is the sensitivity of the sinogram bin defined by r, ϕ. The plane efficiency factor P_{uv} for the plane defined by an LOR connecting detector i from ring u and detector j from ring v is then:

$$P_{u,v} = \frac{\sum_{r,\varphi} S(r,\varphi,u,v)}{\frac{1}{Z^2}\sum_{u,v}\sum_{r,\varphi} S(r,\varphi,u,v)}. \qquad (15)$$

Plane efficiency factors are even more important for the case of barrel-shaped detectors. In these configurations, the axial block rings form small polar angles with each other. Therefore, the axial rings in one block are placed horizontally, but rings belonging to different blocks are not.

Finally, it is important and it should be noted that the plane efficiency correction is also dependent on the data compression scheme used by the reconstruction. Michelogram spanning will affect the correction, based on the maximum ring difference. There are systems in which the LORs are acquired individually, whereas others combine LORs during reconstruction.

Radial geometric factor G_{uvr}

The radial geometric factor is calculated to account for the systematic variation in LOR efficiency with the radial position r in a particular projection. More specifically, for the case of a homogeneous cylindrical source, experiments showed that LOR efficiency is higher toward the edge of the FoV compared with the ones in the

middle [27,30]. This is mainly because, moving toward the edge, the LORs form increasingly oblique angles of incidence on the face of the detector. Oblique angles result in a higher amount of scintillator substance being encountered by the γ rays and in a further increase in the detection probability. In addition, oblique angles of incidence also result in a displacement of the events toward the center. The γ rays penetrate the face of a specific crystal, but because of their excessive energy they finally reach neighboring crystals and are therefore detected from them. Moreover, the solid-angle increase while moving to the edge has a similar impact. The curvature of the ring results in smaller crystal-to-crystal distance as the distance from the center is higher. The solid angle subtended is therefore increased, together with the efficiency of the relevant LOR. The solid-angle effects on the LOR efficiency are well documented in publications on reconstruction algorithms that use solid-angle geometric models [31].

The radial geometric factor is calculated by summing the LOR with the same radial distance r from the different projections and dividing this sum with the number of projections N_ϕ:

$$G_{uvr} = \frac{1}{N_\varphi} \times \left[\frac{1}{Z^2} \times \sum\nolimits_{u,v}^{\mathrm{N}_\varphi - 1} \frac{S(r, \varphi, u, v)}{P_{u,v}} \right], \qquad (16)$$

for the case of a multiring detector with Z rings.

Equation (16) shows the calculation. The set of LORs forming the vertical projection ($\phi = 0^\circ$) is actually rotated to form the rest of the projections (Fig. 8a and b). The projections for $\phi = 45^\circ$ and $\phi = 90^\circ$ are also shown (Fig. 8c and d). Then, for the example, the calculation of the geometrical factor of radial distance r would be the sum of all LORs with the same index (1…16) divided by the number of views N_ϕ (64 for the example in Fig. 4b).

A common finding related to the calculation of the radial geometric factor was verified independently by different researchers [27,32]. The radial geometric profiles revealed a dip in efficiency close to the center of the FoV. This is attributed to the big percentage of LOR collinearity with the slots between the crystals when the annihilations occur near the center. The higher the percentage of the whole detector surface area occupied by the gaps between the blocks and the slots between the crystals, the more intense the dip.

Crystal interference d_{uvrk}

LOR sensitivity variations are strongly dependent on the radial distance of the LOR from the center of the FoV. These variations are accounted for by the radial geometric factors, as already mentioned. However, experiments revealed further remaining variations transaxially, even after the radial geometric factors have been applied. The intensity of these variations followed a periodic pattern with a frequency equal to the transaxial number of crystals in a block. Therefore, it was made clear that the LOR efficiency is dependent not only on the radial distance but also on the respective position of the crystal pair in the block. To state it in a simpler way, two LORs with the same radial distance will be efficiently different if the crystals that they connect are in a different place relevant to the block, even after the block profile has been accounted for. For example, consider LOR_1 and LOR_2 with the same radial distance from the center (Fig. 9). In this case the distance is zero with both lines crossing the center. These LORs will have a different response. LOR_1 connects edge crystals (both crystals are indexed as 1 in the blocks), whereas LOR_2 connects median crystals (indexed as 2 in the blocks). The interference profile for each crystal ($k = 1 \ldots 4$) is different and this is the underlying cause behind the need for crystal interference correction. More specifically, median crystals ($k = 2, 3$) are less efficient than edge crystals ($k = 1, 4$) because of their intense interference profile with their nearest neighbors. The effect is more pronounced for block designs with a bigger number of transaxial crystals.

There is one crystal interference factor for each transaxial crystal index in a block. For the case of the example there are four transaxial crystals in each block ($k = 1 \ldots 4$) and the ring consists of 16 blocks. There are totally 64 crystals in each ring. To calculate the factor for the set of parameters $r = 0$, $k = 1$, and $u = v = 1$ (crystals belong to the same axial ring), first the summation of equidistant LORs for all 16 crystal pairs with $k = 1$ is calculated, and then the result is divided by the number of $k = 1$ crystal pairs in the ring. The calculation also takes into account the plane and radial geometrical factors. In this way, the crystal interference effect will be isolated and will ensure that the crystal interference correction accounts for the remaining variations. The general formula for the calculation is as follows:

$$d_{uvrk} = \frac{1}{N/D} \sum\nolimits_{\varphi=1}^{\frac{N}{D}} \frac{S(r, \left[k + (\varphi - 1) \times D_{u,v}\right]}{P_{u,v} \times G_{uvr}}. \qquad (17)$$

Time window alignment factor t_{ijuv}

The signals from the blocks are taken up by electronics for further processing. Time jitter between the blocks can vary, and this poses a severe impact on the coincidence timing resolution of the system. The processor responsible for categorizing the events as coincident or not will bias the results in the case of timing discrepancies between the blocks. Thus, a time window alignment factor should be applied to account for the effect. The calculation can utilize testing pulses of known characteristics sent to the electronics, simulating the real pulses coming from the events. The number of coincident responses registered from the processor should then be equal for all the blocks, allowing at the same time calculation of the factors that are needed to compensate. The details of such an approach used in systems utilizing

Fig. 8

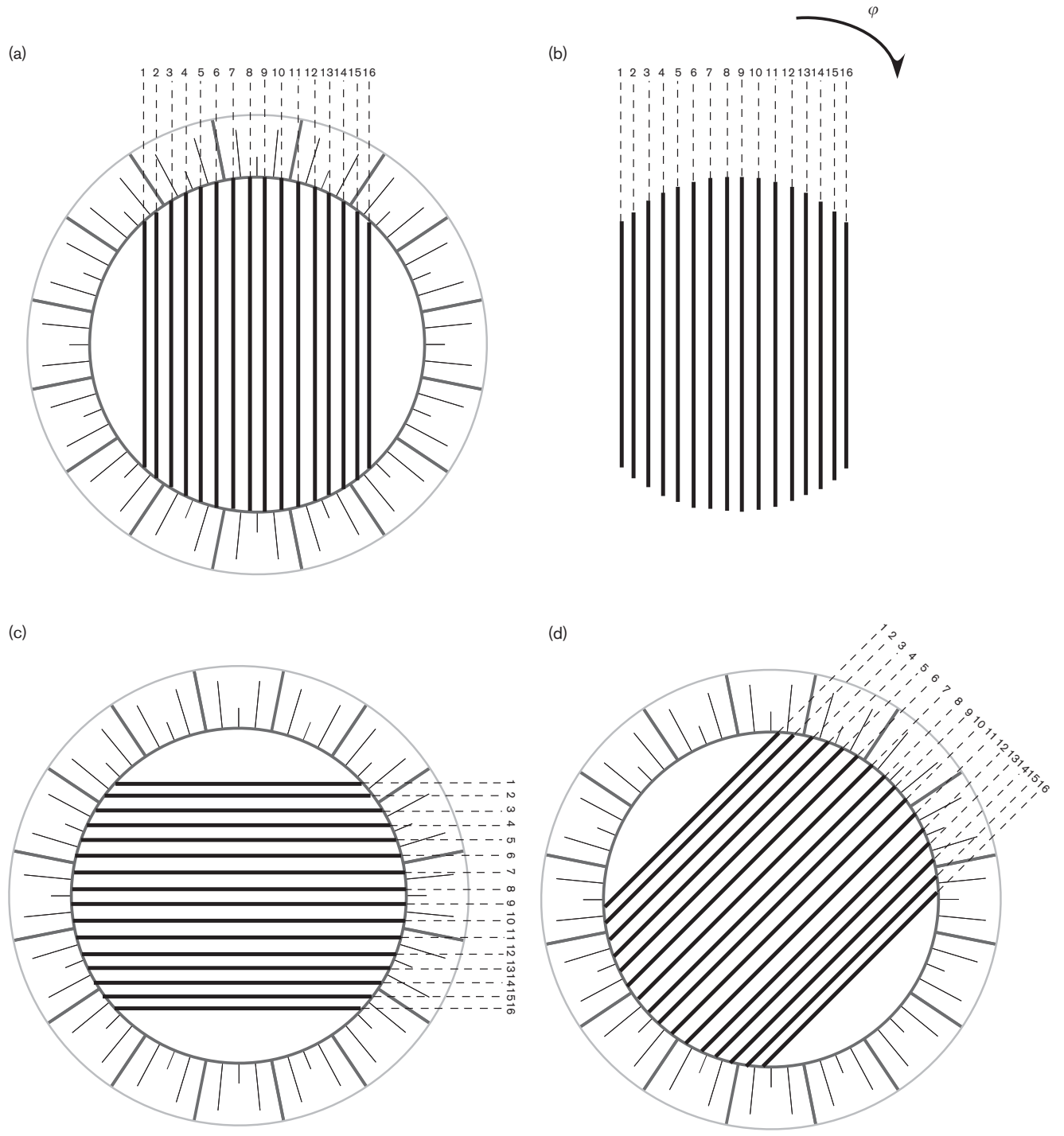

(a) The set of lines of response (LOR) for the different distances from the center forming projection $\phi = 0^\circ$. (b) The same set is rotated to form the rest of the projections like (c) the projection for $\phi = 90^\circ$ and (d) $\phi = 45^\circ$. The calculation of the radial geometric factors starts with the sum of the LOR with the same index (1…16) and for all the projections N_ϕ.

time-of-flight (ToF) reconstruction can be found in Conti *et al.* [33]. In the case of ToF, time alignment factors should be accurately defined because of increasingly stringent temporal resolution demands.

The evolution of the algorithm

Casey and Hoffman [16] derived a method that increased the statistical accuracy of the calculation for random subtraction. Their method was also applied for normal-

Fig. 9

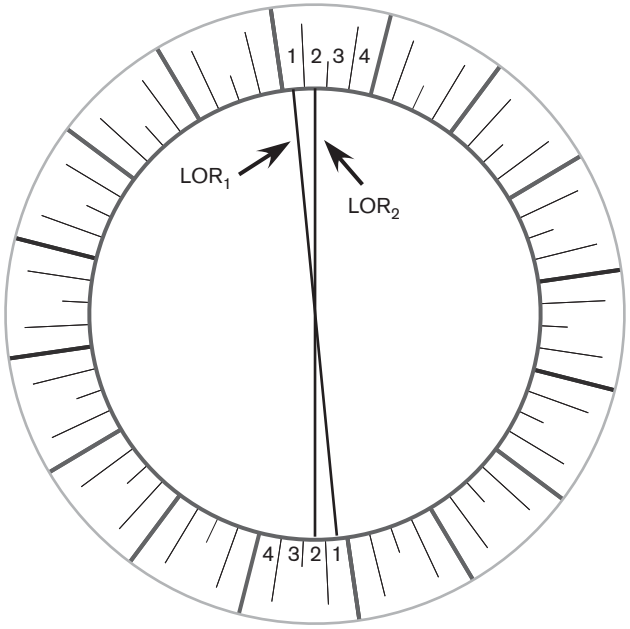

The underlying cause behind the crystal interference effect. LOR_1 and LOR_2 are efficiently different because of their relative position with respect to the block, although they have the same radial distance r from the center of the field of view ($r=0$ in this case). LOR, lines of response.

ization data by virtue of the similarity of the mathematical expression defining random count rate [Eq. (18)] and LOR efficiency [Eq. (19)] for a detector pair. If $C_{ijuv(\mathrm{rand})}$ and C_{ijuv} are the random and true count rates between detector pairs i and j from separate rings u and v, respectively, then:

$$C_{ijuv(\mathrm{rand})} = C_{iu} \times C_{jv} \times 2\tau, \tag{18}$$

$$C_{ijuv} = \varepsilon_{iu} \times \varepsilon_{jv} \times A_0, \tag{19}$$

where C_{iu} and C_{jv} are singles rates for the detectors and 2τ is the coincidence time window. This was actually a variance reduction technique based on two assumptions. The first is that the total random count rate and total activity for a single detector element in coincidence with an opposing fan of detectors are almost constant for all single detector elements in a ring. The second is that geometrical variances of efficiency are considered negligible assuming fans of a relatively small number of elements. The improvement in the calculation using the technique was verified experimentally by comparing the frequency distribution of percentage deviations of a low count normalization scan from a high statistics reference scan with and without applying the method. The importance of the method was apparent because it proved that normalization scans would be possible with fewer counts in less time, without compromising the accuracy of the results. Practically, this would mean that if the size of the accepted fan in coincidence with a single detector is $S = 504$ then the improvement in noise would be equal to $S^2/2S + 1 = 251.75$; hence, the normalization of the detector would be ~ 250 times faster compared with the time needed to perform the direct method. Hoffman *et al.* [22] used this method and introduced the electronic FoV for the normalization scan. They used a uniform 22 cm ^{68}Ge cylinder and estimated normalization factors for the whole bore diameter of their system (29 cm) using extrapolation, thus dealing with image artifacts at the edge of the FoV. They also took into account systematic variations in detector pair efficiency due to circular geometry, which was actually the radial geometric factor. Their model in its simplified version included corrections for the total mispositioning due to geometry and parallax. In their study, the activity correction is included in the geometric factor.

Transition to 3D acquisition mode increased the number of LORs by a factor that depends on the geometry and the effective FoV in the axial direction. This increase resulted in a subsequent increase in the time for acquiring a normalization scan that could deliver accurate results. Defrise *et al.* [32] proved that a high count normalization scan operated in 2D mode could be used for the normalization of detector pairs in 3D mode. To do that, the authors included in their model a new factor that ruled out the effects of the extended septa of the 2D scan, named after septa shadowing. Using the notation of previous equations:

$$C_{ijuv} = \varepsilon_{iu} \times \varepsilon_{jv} \times G_{ijuv} \times q_u \times q_v, \tag{20}$$

where q_u and q_v are scaling factors that can be determined for each ring by taking the ratio of the total count rate of two sinograms. One sinogram measurement was performed with the septa extended and the second with the septa retracted.

Liow *et al.* [34], on the basis of the findings of the previous study, investigated the feasibility of replacing the 2D blank scan that Defrise *et al.* [32] had used in their normalization approach with a 3D blank scan. The setup for the measurements consisted of two rod sources, and the scan was performed with septa retracted. Reconstructed images from phantoms normalized with the 3D technique yielded slightly improved results, and therefore the feasibility of the method was proven. The motivation from the beginning to replace the 2D normalization technique with a 3D scan was that, in this way, the quantification of the final PET images would be more accurate because of no 'septa shadowing effects'. Furthermore, normalizing with the rod sources preserved scatter in the emission data, making the subsequent scatter correction effort easier. One more important finding from this study that should be noted is that, independent of the type of scan used for normalization purposes, no relying results came up when the dead-time factor exceeded 2.5. Therefore, it was clear that, irrespective

of the source setup to be used, the activity level should always be constrained from dead-time effects.

Casey *et al.* [27] presented a newer version of component-based normalization. The study focused on the storage of the individual normalization components – namely, the individual detector efficiencies and the geometrical factor. In this way a mode-specific normalization could be established. The geometric factor that they used encompassed the crystal interference patterns depending on the position of the detector elements in the array. Dead-time parameterization to account for the block profile was also included in the method, and the measurements were taken with a 'pseudoplane' rotating source. Scatter contribution was also investigated. Artifacts arising in the reconstructed images after correcting with the normalization matrix were removed by separately applying the interference and crystal efficiency corrections before scatter correction and the radial geometric correction thereafter. The findings were in agreement with those in a thorough study of this kind for scatter contribution performed by Ollinger [35]. Kinahan *et al.* [20] compared 3D reconstructions of a uniform cylinder with normalization applied using different source geometries. They found that the use of normalization data sets they came up with using a 'pseudoplane' travelling rod source and a uniform cylinder did not reveal statistically significant differences in the final quantitative image. Stearns in his patent [36] also used a 2D normalization scan to calculate the geometrical factors after proper rebinning. In his method, the crystal efficiencies corrected for interference were produced from a 3D uniform cylinder source with the difference being that the projection plane for this acquisition was limited to cover only the source.

The majority of investigations agreed that using 2D normalization data sets for 3D acquisitions resulted in unwanted distortions in the image mostly because of count rate differences between 2D and 3D modes and the effects of septa on the efficiency of corner detectors. One workaround was the use of low-scatter 'pseudoplanar' moving line sources [37]. Oakes *et al.* [38] used this 'pseudoplanar' source and investigated how inaccuracies of the normalization components in their algorithm provoke error propagation through the reconstructed image. Hermansen *et al.* [18] also dealt with the extension of the normalization sinogram measured with a plane source of smaller length than with the transaxial length of the FoV. They allocated the total geometric component into two parts: one depending solely on the distance of the LOR from the center of the FoV and the other, a more complex one, incorporating all the other geometrical effects. Their finding was that, on correcting for the first part, the maximum residual coefficient of variation resulting from the second part is 4%. Thus, if the extended sinogram was created by taking into account only effects due to the distance from the center of the FoV, then a relative root mean square error of 4% is to be expected. An evaluation of the algorithms proposed by Hoffman *et al.* [22] and developed by Casey *et al.* [27] and Defrise *et al.* [32] with some modifications is presented by Badawi *et al.* [26]. Their normalization model was extended and included separate components for the axial and transaxial interference pattern in addition to a plane efficiency factor for cross-plane combinations in 3D acquisition. The geometric factors are calculated separately using a scanning line source, and with this correction already applied the model is limited to the crystal efficiencies. The study focuses not only on the comparison of the algorithms but also on the accuracy of the results that these methods deliver when their 'single-plane' version or their 'multiring' cross-plane version is used. The latter is proven to yield faster acquisition normalization times. In this work it is clearly stated that count rate effects have not been taken into account. They are, however, taken into account in a later study by Badawi *et al.* [39]. A new factor until then, the time alignment factor in the normalization model, is introduced to account for jitter through the electronics processing the signals from the detectors in a block level. This model is a rather detailed one in the sense that it uses separate factors for the differences in efficiencies of the crystals that depend on their position in the block detector. For this purpose, block profile and crystal interference factors are incorporated in the model.

In the same study, it is mentioned that the components of the normalization model can be categorized as fixed, variable, and count rate dependent. The components of the third category should be accompanied by an extra dead-time correction. The authors evaluated the significance of the contribution that each one of the normalization factors had in the final reconstructed image, and came to the conclusion that count rate dependencies could generally be ignored in the context of everyday clinical practice. In contrast, failure to correct for fixed components can lead to high-frequency artifacts. Following this study, Badawi *et al.* [17] implemented several normalization methods in three different clinical scanners. Design characteristics and different grouping schemes for the detectors of the three systems are commented upon. A detailed description of the sequential steps performed during normalization is also included in the study for each system separately, thus providing an example of different approaches for the algorithms adopted.

Special normalization modes

Except from the above models, several other modes of normalization have been presented [40]. Histogrammed list mode data, for example, are first saved as an array during acquisition and reconstruction initiates after the completion of the data set acquisition. This acquisition mode should be approached differently, and attention should be paid to deciding at which stage normalization should be introduced.

Thielemans *et al.* [41] concluded that the noise in the final reconstructed image is greatly reduced by performing the normalization after the binning. Other approaches refer to different detector configurations than the one described above. Algorithms are developed for nonblock design ring scanners [42], detectors with depth of interaction measurement capability [43,44], or for panel detector configurations [45]. Finally, results from simulated data using Monte Carlo simulations proved that the normalization factors should also be taken into account even for simulated data [46]. In this study, the authors conclude that component-based normalization is considered essential to achieve reliable and accurate results from the simulations.

Future aspects

Hybrid imaging involves continuous development and innovation. Following these innovations, data correction strategies are bound to follow. Hardware changes in the detector, or new reconstruction algorithms, yield new requirements for robust normalization approaches toward image quantification. ToF during reconstruction is already available in clinical systems offering higher performances in terms of contrast and noise [47–49]. Additional time bins for ToF-capable systems result in a larger workload for the calculation of normalization components and tighter acceptable precision for time alignment factors in Eq. (8).

At present there is increasing interest on special research into micro-PET systems. The dimensions of the FoV tend to increase together with the total number of crystals, while the complexity of the systems requires ad-hoc normalization strategies for the detector [50–52].

It is evident that normalization correction plays a major role in improved performance of nuclear medical imaging equipment. The development of this technique has proven to be an ongoing effort, with the successful completion of each step a prerequisite to progress to the next phase.

Acknowledgements

Conflicts of interest

There are no conflicts of interest.

References

1 Kapoor V, McCook BM, Torok FS. An introduction to PET/CT imaging. *Radiographics* 2004; **24**:523–543.
2 Kitson SL, Cuccurullo V, Ciarmiello A, Salvo D, Mansi L. Clinical applications of positron emission tomography (PET) imaging in medicine: oncology, brain diseases and cardiology. *Curr Radiopharm* 2009; **2**:224–253.
3 Pichler BJ, Wehrl HF, Judenhofer MS. Latest advances in molecular imaging instrumentation. *J Nucl Med* 2008; **49**:5S–23S.
4 Jones WF, Reed J, Everman J, Luk P, Gremillion T, Castleberry B, *et al.* First time measurement of transaxial resolution for a new high-sensitivity PET prototype using 5 LSO panel detectors. *IEEE Nucl Sci Symp* 2002; **2**:694–698.
5 Gambhir SS, Czernin J, Schwimmer J, Silverman DH, Coleman RE, Phelps ME. A tabulated summary of the FDG PET literature. *J Nucl Med* 2001; **42**:1S–93S.
6 Beyer T, Antoch G, Muller S, Egelhof T, Freudenberg LS, Debatin J, Bockisch A. Acquisition protocol considerations for combined PET/CT. *J Nucl Med* 2004; **45**:25S–35S.
7 Blodgett TM, Meltzer CC, Townsend DW. PET CT: form and function. *Radiology* 2007; **242**:360–385.
8 Ollinger JM. Model-based scatter correction for fully 3D PET. *Phys Med Biol* 1996; **41**:153–176.
9 Watson CC. New, faster, image-based scatter correction for 3D PET. *IEEE Nucl Sci Symp* 1999; **3**:1637–1641.
10 Brasse D, Kinahan PE, Lartizien C, Comtat C, Casey M, Michel C. Correction methods for random coincidences in fully 3D whole-body PET: impact on data and image quality. *J Nucl Med* 2005; **46**:859–867.
11 Amamoto SY, Orii HH, Urutani MH, Atsumoto KM, Enda MS. Investigation of single, random, and true counts from natural radioactivity in LSO-based clinical PET. *Ann Nucl Med* 2005; **19**:109–114.
12 Kinahan PE, Townsend DW, Beyer T, Sashin D. Attenuation correction for a combined 3D PET/CT scanner. *Med Phys* 1998; **25**:2046–2053.
13 Reza MA, Zaidi H. Assessment of errors caused by X-ray scatter and use of contrast medium when using CT-based attenuation correction in PET. *Eur J Nucl Med Mol Imaging* 2006; **33**:1301–1313.
14 Badawi RD, Miller MP, Bailey DL, Marsden PK. Randoms variance reduction in 3D PET. *Phys Med Biol* 1999; **44**:941–954.
15 Ziegler SI. Positron emission tomography: principles, technology, and recent developments. *Nucl Phys A* 2005; **752**:679c–687c.
16 Casey ME, Hoffman EJ. Quantitation in positron emission computed tomography: 7. A technique to reduce noise in accidental coincidence measurements and coincidence efficiency calibration. *J Comput Assist Tomogr* 1986; **10**:845–850.
17 Badawi RD, Ferreira NC, Kohlmyer SG, Dahlbom M, Marsden PK, Lewellen TK. A comparison of normalization effects on three whole-body cylindrical 3D PET systems. *Phys Med Biol* 2000; **45**:3253–3266.
18 Hermansen F, Spinks TJ, Camici PG, Lammertsma AA. Calculation of single detector efficiencies and extension of the normalization sinogram in PET. *Phys Med Biol* 1997; **42**:1143–1154.
19 Vicente E, Vaquero JJ, España S, Herraiz JL, Udías JM, Desco M. Normalization in 3D PET: dependence on the activity distribution of the source. *IEEE Nucl Sci Symp* 2006; **4**:2206–2209.
20 Kinahan PE, Townsend DW, Bailey DL, Sashin D, Jadali F, Mintun MA. Efficiency normalization techniques for 3D PET data. *IEEE Nucl Sci Symp* 1995; **2**:1021–1025.
21 Wollenweber SD, McDaniel DL, Stearns CW. Dead-time correction for a rotating rod normalization in a cylindrical PET system. *IEEE Nucl Sci Symp* 2003; **3**:2222–2226.
22 Hoffman EJ, Guerrero TM, Germano G, Digby WM, Dahlbom M. PET system calibrations and corrections for quantitative and spatially accurate images. *IEEE Trans Nucl Sci* 1989; **36**:1108–1112.
23 Cherry SR, Tornai MP, Levin CS, Siegel S, Hoffman EJ. A comparison of PET detector modules employing rectangular and round photomultiplier tubes. *IEEE Trans Nucl Sci* 1995; **42**:1064–1068.
24 Salomon A, Goldschmidt B, Botnar R, Kiessling F, Schulz V. A self-normalization reconstruction technique for PET scans using the positron emission data. *IEEE Trans Med Imaging* 2011; **31**:2234–2240.
25 Stazyk MW, Sossi V, Buckley KR, Ruth TJ. Normalization measurement in septa-less PET cameras. *J Nucl Med* 1994; **35**:41–49.
26 Badawi RD, Lodge MA, Marsden PK. Algorithms for calculating detector efficiency normalization coefficients for true coincidences in 3D PET. *Phys Med Biol* 1998; **43**:189–205.
27 Casey ME, Gadagkar H, Newport D. A component based method for normalization in volume PET. International meeting on fully 3D image reconstruction in radiology and nuclear medicine; 4–6 July 1995, Aix-les-Bains, France. Available at: *http://fully3d.org/old_meetings.html*. [Accessed 2 February 2012].
28 Badawi RD, Marsden PK. Self-normalization of emission data in 3D PET. *IEEE Trans Nucl Sci* 1999; **46**:709–712.
29 Ishikawa A, Kitamura K, Mizuta T, Tanaka K, Amano M. Self normalization for continuous 3D whole body emission data in 3D PET. *IEEE Nucl Sci Symp* 2004; **6**:3634–3637.
30 Bailey DL, Townsend DW, Valk P, Maisey M. *Positron emission tomography*. London: Springer-Verlag; 2004.
31 Liu CC, Hsu CH, Hsiao IT, Lin KM. Effect of geometric models on convergence rate in iterative PET image reconstructions. *J Instrum* 2009; **4**:5–10.
32 Defrise M, Townsend DW, Bailey DL, Geissbuhler A, Michell C, Jones T. A normalization technique for 3D PET data. *Phys Med Biol* 1991; **36**:939–952.
33 Conti M, Bendriem B, Casey M, Chen M, Kehren F, Michel C, *et al.* First experimental results of time-of-flight reconstruction on an LSO PET scanner. *Phys Med Biol* 2005; **50**:4507–4526.

34 Liow JS, Strother SC. Normalization using rotating rods for 3D PET. International meeting on fully 3D image reconstruction in radiology and nuclear medicine; 4–6 July 1995, Aix-les-Bains, France. Available at: *http://fully3d.org/old_meetings.html*. [Accessed 2 February 2012].

35 Ollinger JM. Detector efficiency and compton scatter in fully 3D PET. *IEEE Trans Nucl Sci* 1995; **42**:1168–1173.

36 Stearns CW. Method for determining data normalization factors for image reconstruction. US patent No. 5 543 622; 1996.

37 Bailey DL, Townsend DW, Kinahan PE, Grootoonk S, Jones T. An investigation of factors affecting detector and geometric correction in normalization of 3D PET data. *IEEE Nucl Sci Symp* 1995; **2**:997–1001.

38 Oakes TR, Sossi V, Ruth TJ. Normalization for 3D PET with a low-scatter planar source and measured geometric factors. *Phys Med Biol* 1998; **43**:961–972.

39 Badawi RD, Marsden PK. Developments in component-based normalization for 3D PET. *Phys Med Biol* 1999; **44**:571–594.

40 Bai B, Li Q, Holdsworth CH, Asma E, Tai YC, Chatziioannou A, Leahy RM. Model-based normalization for iterative 3D PET image reconstruction. *Phys Med Biol* 2002; **47**:2773–2784.

41 Thielemans K, Morel C, Jacobson MW, Kaempf JH, Mustafovic S. Normalisation of histogrammed list mode data. *IEEE Trans Nucl Sci* 2008; **55**:543–551.

42 Wang W, Hu Z, Gagnon D. A new component approach efficiency normalization for 3D PET. *IEEE Trans Nucl Sci* 2007; **54**:92–99.

43 Foudray AMK, Chinn G, Levin CS. Component based normalization for PET systems with depth of interaction measurement capability. *IEEE Nucl Sci Symp* 2005;2108–2111.

44 Sibomana M, Keller SH, Holm S, Bloomfield PM, Blinder S, Hansen SB, Michel C. Component-based normalization for the HRRT for sinogram-mode reconstruction. *IEEE Nucl Sci Symp* 2009; **1**:2694–2697.

45 Conti M, Hamill JJ, Casey ME, Chen M. Normalization apparatus for panel detector PET scanners. US patent No. 6 963 065; 2005.

46 Pepin A, Stute S, Jan S, Comtat C. Normalization of Monte Carlo PET data using Gate. *IEEE Nucl Sci Symp* 2011; **21S**:4196–4200.

47 Cui J, Pratx G, Prevrhal S, Levin CS. Fully 3D list-mode time-of-flight PET image reconstruction on GPUs using CUDA. *Med Phys* 2011; **38**:6775–6786.

48 Panin VY. Iterative algorithms for crystal efficiencies estimations from time of flight compressed normalization data. US patent No. US2010/0072375 A1; 2010.

49 Karp JS, Surti S, Daube-Witherspoon ME, Muehllehner G. Benefit of time-of-flight in PET: experimental and clinical results. *J Nucl Med* 2008; **49**:462–470.

50 Visser EP, Disselhorst JA, Laverman P, Gotthardt M, Oyen JG, Boerman OC. Contribution of normalization to image noise for the Siemens Inveon small-animal PET scanner. *Nucl Instrum Methods A* 2009; **605**:433–435.

51 Camborde M, Rhamim A, Newport DF, Siegel S, Buckley KR, Vandervoort E, *et al*. Effect of normalization method on image uniformity and binding potential estimates on microPET. *IEEE Nucl Sci Symp* 2004; **6**: 3467–3471.

52 Yang Y, Tai Y, Siegel S, Newport DF, Bai B, Li Q, *et al*. Optimization and performance evaluation of the microPET II scanner for in vivo small-animal imaging. *Phys Med Biol* 2004; **49**:2527–2545.